Radiotherapy drives lung metastasis in PDAC via a RhoGTPase signaling shift towards MRCK-dependency

McLay KM[1†], Tesson M[2†], Dutton L[1], Sun Y, Misquitta JD[1], Stevenson K[1], Corbyn R[2], Lilla S[2], McGarry L[2], Maka N[1], Shaw R[2], Miller C[1,2], Carlin LM[1,2], Chalmers AJ[1], Olson MF[3], Morton JP[1,2¥], Birch JL [1¥*]

[1] School of Cancer Sciences, University of Glasgow, UK

[2]CRUK Scotland Institute, Glasgow, UK

[3]Toronto Metropolitan University, Toronto, Canada

*Address for correspondence. Dr Joanna Birch, Wolfson Wohl Translational Cancer Research Centre, School of Cancer Sciences, University of Glasgow, UK. Email Joanna.birch@glasgow.ac.uk.

†, ¥ Authors have made an equal contribution

No conflicts of interest declared.

Word count: Abstract 183, main text 4998

Abstract

Pancreatic ductal adenocarcinoma (PDAC) is an aggressive cancer with an extremely poor prognosis, partly owing to its highly metastatic nature. Although radiotherapy is an effective and potentially curative treatment modality, research over the last few decades has indicated that it may induce a more metastatic phenotype in surviving cancer cells. We demonstrate for the first time that clinically relevant doses of image-guided targeted radiotherapy induce metastasis in a genetically engineered KPC mouse model of PDAC. Furthermore, this induction is largely driven by an organotropic switch towards lung metastasis. Using an *in vitro* RNAi screening approach, we identified a key role for myotonic dystrophy-related Cdc42-binding kinase (MRCK) in driving this response. MRCK activity was spatially upregulated at the plasma membrane in response to radiotherapy in PDAC cell lines as well as at the invasive margins of PDAC tumors. This upregulation of activity was maintained in metastases, suggesting an important role for MRCK in not only triggering local invasion in response to radiotherapy but also promoting distant metastases. Importantly, inhibition of MRCK with a small-molecule inhibitor (BDP9066) specifically opposed radiation-driven MRCK upregulation and pro-metastatic response.

58

59

60 **Introduction**

61 Pancreatic ductal adenocarcinoma (PDAC) is a highly aggressive and metastatic malignancy with a
62 dismal five-year survival rate of less than 10% (1). Despite the low incidence rates, it is projected to
63 become the second leading cause of cancer-related death within the next five years with survival
64 outcomes having not significantly improved since the 1970s, highlighting the urgent need for novel
65 therapeutic strategies (2). PDAC is largely refractory to current treatments, and surgical resection is
66 the only potentially curative option. Chemotherapy offers only modest survival benefits, leading to a
67 dismal median survival of less than six months (3). The role of radiotherapy (RT) in PDAC treatment
68 remains controversial owing to inconsistent clinical trial outcomes regarding its efficacy. While some
69 evidence suggests improved overall survival in the neoadjuvant setting, as demonstrated by the
70 PREOPANC phase III trial, in which a gemcitabine-based chemoradiotherapy regimen resulted in
71 superior survival outcomes compared to upfront surgery and gemcitabine alone in resectable and
72 borderline-resectable cases, other studies have reported conflicting findings (4,5). The LAP07 trial, for
73 instance, demonstrated that although chemoradiation delayed local tumor progression in locally
74 advanced PDAC, it did not confer an overall survival advantage (6). As a result, the current
75 recommendation is for RT to be utilized in patients who are poor surgical candidates or have locally
76 advanced disease (7).

77 The limited efficacy of RT in PDAC can be partially attributed to its intrinsic radioresistance, which
78 arises from a dense, fibrotic, and immunosuppressive tumor microenvironment with acquired
79 resistance mechanisms that also contribute to treatment failure (8,9). Another factor that may impact
80 the lack of efficacy is RT-induced invasion and metastasis, a phenomenon that has been documented
81 preclinically in multiple malignancies and reviewed in various articles (10-12). However, despite
82 growing evidence supporting this phenotype in other malignancies, studies investigating RT-induced
83 metastasis in PDAC have largely been confined to *in vitro* analyses, with no *in vivo* preclinical studies
84 investigating its impact on the metastatic burden in clinically relevant models (13,14).

85 RhoGTPases are a family of 26 signaling proteins that drive actin cytoskeletal dynamics to promote
86 cell migration and invasion and consequently play a critical role in tumor metastasis (15,16).
87 Downstream signaling from RhoGTPases is mediated by a panel of effector kinases, including LIM
88 domain kinase (LIMK), Rho-associated protein kinase (ROCK), and myotonic dystrophy kinase-related
89 Cdc42-binding kinase (MRCK), to create a complex and dynamic network (17-19). This complexity

leads to a high degree of plasticity that allows cells to adapt to changing conditions within the microenvironment (ME). For example, the RhoA-ROCK signaling axis is used by cells to adopt amoeboid migration to allow navigation through small gaps in the stroma. However, when this form of migration is insufficient to allow cells to pass through dense, complex stroma, cells can switch to a Rac1/CDC42-MRCK driven mesenchymal phenotype that allows extracellular matrix (ECM) degradation and pseudopod formation (20,21).

Interestingly, the RhoA-ROCK axis has been demonstrated to drive invasion in preclinical studies of PDAC under physiological conditions, although how the network responds to radiotherapy to support metastasis remains to be elucidated (19). In glioblastoma, a tumor in which cells adopt a more mesenchymal mode of invasion, MRCK was demonstrated to drive local dissemination of disease under standard of care radiotherapy in preclinical models (22,23). However, the role of other RhoGTPase members and downstream effectors in supporting invasion and metastasis is yet to be comprehensively assessed under physiological or irradiated conditions.

In this study, we demonstrated a pro-migratory phenotype induced by RT in multiple PDAC cell lines. Importantly, we demonstrated for the first time that this increased motility correlates with a significant increase in metastatic burden in a clinically relevant PDAC model, with a tropism switch to the lung. We showed that this effect is mediated by altered RhoGTPase signaling, with RT promoting a dependency on MRCKα signaling to drive the pro-invasive phenotype. Specifically, we showed that RT increases MRCK activity both *in vitro* and *in vivo*, with spatially localized activation at the invasive edge of irradiated KPC tumors and metastases. Furthermore, both RNAi and pharmacological inhibition of MRCK significantly inhibited RT-induced motility, highlighting the potential of anti-invasive strategies for improving RT efficacy. Importantly, given the established role of MRCK in RT-induced invasion of other malignancies, our findings suggest that MRCK signaling may represent a more central mechanism underlying RT-induced invasion across different cancer types.

Materials and Methods

Cell culture

cell lines were maintained in incubators at 37°C with 5% CO_2, tested regularly for mycoplasma, and authenticated using STR profiling. The PANC-1 (male) and MiaPaCa-1 (female) cell lines were cultured in DMEM (ThermoFisher Scientific #21969035) supplemented with 10% FBS, 1% penicillin/streptomycin (ThermoFisher Scientific 15140-122) and 2mM L-glutamine (ThermoFisher Scientific #25030-024). AsPC-1 cells (female) were cultured in RPMI 1640 medium (ThermoFisher

123 Scientific #11875093) supplemented with 10% FBS, 1% penicillin/streptomycin (ThermoFisher
124 Scientific #15140- 122) and 2mM L-glutamine (ThermoFisher Scientific #25030-024). NBC12.2f
125 (female), NBC12.2g (female), and NBC13.3a (male) murine cell lines were generated in-house from
126 C57Bl/6 KPC mice and cultured in DMEM supplemented with 10% FBS, 1% Penicillin/Streptomycin and
127 2mM L-glutamine. The primary patient lines, TKCC04 and TKCC05, were kindly gifted by Professor
128 David Chang (University of Glasgow), were characterized as the squamous subtype, and were cultured
129 in RPMI 1640 medium (ThermoFisher #11875093) supplemented with 10% FBS, and 20ng/mL
130 Epidermal Growth Factor (Life Technologies #PHG0311L) (24).
131
132 **Subconfluent migration assay**
133 Cells (1×10^4 cells/mL) were seeded in an appropriate culture dish for the experimental assay (35 mm
134 dishes or 12-well plates) and left to adhere for 24hours. Drug treatments and irradiation were carried
135 out 4 h prior to imaging unless otherwise stated. Timelapse microscopy images were acquired in phase
136 contrast every 20 mins for 16 hours at 10 X magnification (10x/0.30 Plan Fluor Ph1, Nikon). Cell speed
137 was calculated using single-cell tracking performed in ImageJ. All *in vitro* experiments were conducted
138 in biological triplicates, and statistical analysis details are within the corresponding figure legends.
139
140 **Automated cell tracking**
141 Automated tracking was conducted using scripts developed by Dr. Ryan Corbyn (Beatson Advanced
142 Imaging Resource Facility RRID:SCR_023875, CRUK-SI). Time-lapse imaging data were acquired using
143 an IncuCyte S3 system. IncuCyte data was preprocessed to collate the individual time points from the
144 experiment into a single time-lapse image stack followed by drift correction to stabilize the image
145 stacks (Fiji macro “correct 3D drift.”). Bespoke Python scripts were written by Dr. Ryan Corbyn and run
146 in a Jupyter integrated development environment (IDE) for cell segmentation and cell tracking. "We
147 retrained the livecell model from cellpose 2.0 on a subset of the imaging data for automated
148 cell segmentation(25,26). Automated cell tracking was subsequently performed using BTracks,
149 which employs a Bayesian single-cell tracking algorithm and generates deep lineage tree analyses as
150 described by Ulicna et al. ((27)). Tracks of cells present in >90% of the total number of frames were
151 used for further analysis. Further analysis of track lengths and cell speeds was performed for all
152 tracked cells, with the resulting data exported as. csv files.
153
154 **High-throughput immunofluorescence**
155 Cells were seeded at a density of 3×10^3 cells per well in 96-well optically clear plates (Greiner
156 #655892) and allowed to adhere overnight prior to irradiation and/or drug treatments, as specified in

157 the experimental conditions. Treated cells were incubated for an additional 24 h unless otherwise
158 stated. After treatment, the cells were washed with PBS before fixation with 4% formaldehyde at room
159 temperature for 15 min. Cells were permeabilized using 0.1% Triton X-100 in PBS for 10 min, washed
160 with TBS containing 0.1% Tween-20 (TBS-T), and blocked in 1% BSA in TBS-T for 30 min at room
161 temperature. For immunofluorescence staining, cells were incubated with the primary antibody
162 diluted in blocking solution overnight at 4°C. The details of the primary antibodies are listed in Table
163 S1. After primary antibody incubation, cells were washed three times with PBS and then incubated
164 with secondary antibody along with 1:1000 DAPI (Thermo Scientific #D1306), Texas Red-X Phalloidin
165 (Thermo Scientific #T7471) and 1:10,000 HCS CellMask Deep Red Stain (Thermo Scientific #H32721)
166 for 1 h at room temperature. After incubation, the cells were washed and stored in PBS. High-content
167 imaging was performed using the PerkinElmer Opera High-Content Screening System, and image
168 analysis was conducted using the Columbus™ image analysis software.
169
170 **Cell viability assays**
171 Cells were seeded at a density of 1×10^4 cells/mL in 96-well plates (Corning) and allowed to adhere
172 overnight. Cells were irradiated at either 0 or 5 Gy using the Xstrahl RS225 and treated with BDP9066
173 for 24 h. Cell viability was assessed using the CellTiter-Glo® assay (Promega #G9241) and Promega
174 Glomax Multi detection system.
175
176 **siRNA transfections**
177 Cells used for transfection were maintained in medium free of penicillin/streptomycin for at least one
178 week prior to the start of experiments. PANC-1 and Mia PaCa-2 cells were transfected with siRNA
179 targeting CDC42BPA (MRCKα) or control scrambled siRNA (Dharmacon #L003290-00; MRCKα
180 AAGAAUAUCUGCUGUGUUU) using DharmaFECT 2 transfection reagent (Dharmacon #T-2005-01) and
181 incubated for 48 h prior to imaging or protein extraction.
182
183 **Proteome analysis**
184 Fifteen-centimetre dishes were pre-coated with Matrigel prior to cell seeding to increase cell
185 adherence. Matrigel was diluted at a ratio of 1:40 in cold DMEM medium without additional
186 supplements. A total of 5 mL Matrigel dilution was added to each dish and incubated at 37°C and 5%
187 CO_2 for 1 hour. Excess medium was aspirated prior to cell seeding.
188 PANC-1 cells were seeded at a density of 2×10^5 cells/mL in Matrigel-coated dishes, with 15 mL of cell
189 suspension per dish. Three biological replicates were plated. Cells were left to adhere overnight at
190 37°C and 5% CO_2, resulting in ~80% confluency. Six hours before analysis, the media were aspirated,

191 and plates were washed six times with PBS to ensure all cell debris was removed. Media was then
192 replaced with 10mL FBS-free culture medium. Immediately after media replacement, cells were
193 irradiated with either 0 Gy or 5 Gy and incubated for 6 hours. Following this incubation, cell lysates
194 were collected for proteome and secretome analysis, respectively.
195 Ultra-High Performance Liquid Chromatography/Tandem Mass Spectrometry (UHPLC-MS/MS)
196 analysis and data analysis conducted by the CRUKSI proteomics facility. See supplemental data for
197 details.
198
199 **RNAseq**
200 NBC12.2g, NC12.2f and NBC13.3a were irradiated +/- 5 Gy. RNA was extracted 24 hours post
201 irradiation using Rneasy kit (Qiagen) kit. Truseq (Illumina) mRNA-seq libraries were prepared from
202 total RNA and these were then sequenced using the Illumina HiSeq 4000 using 50M read pairs,
203 2x75bp read length. DEseq2 was utilised for differential gene analysis. Volcano plot created in
204 GraphPad Prism v10.60. See supplementary methods for full analysis details.
205
206 **RNAi screen**
207 PANC1 cells were seeded at a density of 1×10^5 cells/mL in two 12-well plates and allowed to adhere
208 overnight. Cells were transfected with 25 nM custom siRNA ON-TARGETplus SMARTpool library
209 (Horizon) using DharmaFECT 2 transfection reagent and incubated overnight. The details of the siRNA
210 are shown in Table S2. After incubation, transfected cells were washed twice with PBS, detached from
211 the wells using TrypLE (250 µL per well), and resuspended in an additional 750 µL of antibiotic-free
212 medium. Cells were plated at a density of 1×10^4 cells/mL in 24-well plates for the subconfluent
213 migration assay. In parallel, selected transfected cells were replated into additional 6-well plates for
214 protein extraction to verify successful knockdown. All replated cells were allowed to adhere overnight
215 at 37°C and 5% CO_2 and subject to 0 Gy or 5 Gy after 16hrs and 4 h prior to imaging.
216
217 **Western blot**
218 Cells were lysed with 1% SDS and 50 mmol/L Tris (pH 6.8) supplemented with protease and
219 phosphatase inhibitors (Thermo Scientific #1861280) followed by SDS-PAGE using 4–12% Novex Bis-
220 Tris gels or 8% BOLT Bis-Tris Plus gels (Thermo Fisher Scientific), and transfer onto nitrocellulose
221 membranes and western blotting with enhanced chemiluminescence (ECL) detection. Primary
222 antibodies were diluted in 5% bovine serum albumin (BSA). The details of the primary antibodies used
223 are shown in Table S1.
224

225 ***In vivo* experiments**

226 All animal work was conducted under the guidance of the UK Home Office regulations and carried out
227 under project license PP8411096. All experiments were approved by the University of Glasgow Animal
228 Welfare and Ethical Review Board. The mice were housed in standard cages with access to food and
229 water *ad libitum*. Environmental enrichment was also provided. KPC mice of both sexes were used in
230 all the experiments. *Pdx1-Cre*; *LSL-Kras*$^{G12D/+}$; *LSL-Trp53*$^{R172H/+}$ (KPC; (28)) mice were bred in-house at
231 the CRUK Scotland Institute, maintained on a mixed background, and genotyped using Transnetyx
232 (Cordoba, TN, USA). The mice were palpated weekly to detect pancreatic tumors, and the presence of
233 a pancreatic tumor was confirmed by 3-dimensional (3D) ultrasound using the Vevo3100 high-
234 frequency ultrasound platform (FUJIFILM VisualSonics) prior to enrolment in the treatment arm. Mice
235 in the treatment group were housed in the same room, and single housing was avoided where
236 possible. In the gemcitabine study, mice were intraperitoneally administered 100 mg/kg gemcitabine
237 twice a week.

238

239 ***In vivo* irradiation of pancreas tumour**

240 The Small Animal Radiotherapy Research Platform (SARRP, Xstrahl) was used to deliver targeted
241 irradiation as previously described (29). Mice were anesthetized using a mixture of medical air and
242 isoflurane for the duration of the radiotherapy session. An iodine contrast-enhanced cone beam
243 computed tomography (CBCT) image was obtained from 1,440 projections using the in-built cone
244 beam CT function of SARRP. To enhance contrast, the mice were administered 0.25 ml Iohexol
245 (Omnipaque™, GE Healthcare) intraperitoneally immediately prior to CT acquisition. Radiotherapy
246 planning was performed using Muriplan software, including tissue segmentation and placement of an
247 isocenter to localize the pancreatic tumor. Arc radiotherapy was delivered at 280 cGy/min (220 kV, 13
248 mA) using three fractions of 4 Gy every other day, three fractions of 6 Gy every other day, or a single
249 fraction of 12 Gy. The collimator aperture size was selected based on tumor shape and size. The mock
250 irradiation controls consisted of mice subjected to 1,440 CBCT acquisitions, which resulted in the
251 delivery of 6.22 cGy (29). Mice were monitored by researchers blinded to the treatment arm and
252 euthanized when they exhibited clinical signs of PDAC (distended abdomen, loss of body conditioning,
253 lethargy, and jaundice).

254

255 **Histology and immunohistochemistry**

256 Tissue samples were fixed in formalin and embedded in paraffin using standard protocols before
257 acquisition of 4 μm sections using a HistoCore MULTICUT microtome (Leica, UK). Tissue sections were
258 placed on poly-L -lysine slides and oven baked at 60 °C for 2 h prior to staining with hematoxylin and

259 eosin (H&E) or immunohistochemistry (IHC) for Zeb1, and pMRCK. The full list of antibodies used is
260 presented in Table S1.
261
262 All liver and lung tissues from control mice and those that received 3 × 4 Gy of radiation were subjected
263 to serial sectioning (five sections at 50 µm intervals). The sections were blinded and double scored for
264 the presence of metastases. For IHC, antigen retrieval and antibody dilution were optimized in-house
265 for each antibody (Table 2.8).
266
267 Automatic quantification of staining was performed using QuPath ((30), v0.05.1). The full slides were
268 scanned and imaged using a Lecia Aperio AT2 slide scanner. Quantification was conducted blinded,
269 with either the full tumor or five areas at the tumor center and tumor border selected at random.
270 These areas were annotated using QuPath annotation tools. The percentage of positive cells was then
271 calculated.
272
273 **Statistical analysis**
274 Statistical analyses are detailed in the figure legends for all experiments. Statistical analyses were
275 performed using the GraphPad Prism software. The number of independent experiments for each in
276 vivo experiment is within the figure legend and refers to experiments repeated on different days with
277 cells at different passages for each cell line reported. Biological repeats refer to independently derived
278 cell lines used as replicates.
279
280 **Data availability**
281 The data generated in this study are publicly available in (https://github.com/Beatson-
282 CompBio/McLay_2025_A/) (AI tracking scripts), https://www.ebi.ac.uk/fg/annotare
283 (RNAseq), http://www.ebi.ac.uk/pride (PXD068500, see supplementory methods for details).
284
285 **Results**
286
287 **Radiotherapy induces motility across a panel of PDAC cell lines**
288
289 Initial qualitative morphological analyses indicated that sublethal doses of RT (5 Gy) induced a shift in
290 morphology of PANC1 cells towards a more elongated shape, reminiscent of a mesenchymal transition
291 (Fig. 1A). Indeed, comprehensive and unbiased high-throughput immunofluorescent imaging and
292 automated analysis indicated that radiotherapy significantly increased the cell area in two PDAC cell
293 lines, which may be indicative of a motile phenotype through increased engagement with integrin
294 signaling (Fig. 1B)(31). Previous studies have reported increased PDAC cell motility *in vitro* in response
295 to RT; however, these studies have been limited in terms of cell line number and available technologies,

296 and as such, have yielded conflicting results ((32-34); as summarized in Table S3). Therefore, we used
297 a comprehensive approach across a panel of commercial, mouse-derived, and primary patient cell
298 lines to measure the effect of RT on PDAC cell motility. We used clinically relevant doses of RT (2 and
299 5 Gy) combined with subconfluent migration assays and single cell tracking to eliminate potential
300 confounding effects on proliferation. We identified a significant increase in migration speed across the
301 selection of three commercial, mouse, and primary lines (Fig. 1C). Parallel cell viability assays indicated
302 that RT had a modest impact on the viability of the TKCC04 line only at this short timepoint (24hrs;
303 Fig.1D). Expansion of this panel indicated that, while the effect of RT on migration is not ubiquitous,
304 five out of eight lines showed increased migration speed post RT, with a further two showing a trend
305 towards an increase (Table 1). Of note, the only murine line that did not show a significant increase in
306 speed, NBC12.2g, was more radiosensitive than the other two lines (Fig. S1).

307

308 **Radiotherapy increases the metastatic burden of pancreatic cancer in a clinically relevant genetic**
309 **mouse model**

310

311 While the activation of cancer cell migration is the initiating step in metastasis, a number of key
312 processes are required within the context of an entire organism, including local extracellular matrix
313 invasion, dissemination via the vasculature/lymph system, and seeding of distant sites. In light of this,
314 we assessed whether the increased motile phenotype translates to an increased metastatic burden *in*
315 *vivo* in a genetically engineered KPC mouse model of PDAC (*LSL-Kras*$^{G12D/+}$; *LSL-Trp53*$^{R172H/+}$; *Pdx1-Cre*)
316 in combination with image-guided targeted RT using a Small Animal Irradiation Platform (SARRP) (Fig.
317 S2A). This model simulates the entire metastatic cascade following targeted irradiation of the primary
318 tumor, allowing us to assess the response to RT in a clinically relevant model and to gain insight into
319 the potential clinical impact of RT on metastasis (Fig. 2A). To ensure a robust analysis, we cut five H&E
320 sections of liver and lungs from control and irradiated (3 × 4 Gy) PDAC mice at 50µm intervals, which
321 were blinded and double scored for the presence of metastases (Fig. 2B). The results indicated that
322 RT induced a significant increase in not only local invasion (Fig. 2C) but also metastatic burden (Fig.
323 2D). Importantly, 3 × 4 Gy did not prolong the survival of KPC mice, as shown in Fig. S2B and previously
324 published data (29), ruling out the possibility that the radiation-associated increase in metastasis may
325 be due to the additional time for tumor cells to seed metastases. In agreement, there was no
326 association between the lifespan of the animal and the presence of metastases on post-mortem
327 examination (Chi Square, P=0.564).
328 Radiotherapy is given in fractionated doses in the clinic, with a trend towards hypofractionation in
329 recent years. To assess whether fraction size and number impact the effect of RT on metastasis, we
330 extended our analysis to include cohorts of mice that received 3 × 6 Gy (increased fraction dose) and

331 1 × 12 Gy (hypofractionation). However, only a significant increase in survival was observed in the 1 x
332 12 Gy cohort (Fig. S2B), all three RT protocols showed a significant pro-metastatic outcome (Fig. 2E),
333 whereas mice treated with gemcitabine alone showed a reduction in metastatic burden (Fig. S2C).
334 These data suggest that RT promotes metastasis independent of the relative lifespan of the treated
335 animals.
336 PDAC metastasizes primarily to the liver and lungs in both patients and the KPC model. Interestingly,
337 and in support of a radiation-specific metastatic induction mechanism, when we analyzed lung and
338 liver metastases separately, we found that RT induced an organotropic switch towards the lungs
339 across all irradiated cohorts (Fig. 2F).
340
341 **RT augments RhoGTPase signaling towards a dependence on MRCK and RhoU**
342 To unpick the potential mechanisms that drive the rapid motility response that we observed post RT
343 and begin to understand how this might trigger the metastatic cascade, we performed RNA-seq and
344 proteomics on PDAC lines post RT/sham RT. There were relatively few genes (at 24h post RT) or
345 proteins (6h post RT) that displayed significant fold changes greater than 1.5 at the relatively short
346 time points used, and no evidence of an emerging motility signature (Fig. 3A-B). This was the case
347 when the cut-off was reduced to a 1.2-fold change in the proteomic data, with response to cellular
348 stress emerging as the main signature post RT (data not shown). Therefore, we sought to undertake a
349 more targeted functional screen of known drivers of motility that are regulated rapidly and
350 independently of gene expression. RhoGTPases drive cancer cell motility and invasion through direct
351 action on the cytoskeleton and are therefore likely to be required to support the observed changes in
352 motility and metastasis.
353 We developed an unbiased, AI-driven, automated segmentation and single-cell tracking approach to
354 assay the dependence of PDAC cells on RhoGTPase family members and associated kinases pre- and
355 post RT for migration (Fig. 3C). To mitigate the inherent plasticity and redundancy in the RhoGTPase
356 network, we used an siRNA approach to transiently knock down each target in PANC1 cells. Using this
357 approach, we achieved knockdown efficiency of approximately 50% across a range of selected targets
358 (Western blot analysis; Fig. 3C(i); Fig. S3). The results in Fig. 3D indicate that there is an overall shift
359 towards dependency upon RhoGTPase activity for motility following RT, with a significant interaction
360 between the presence or absence of RT and the ablation of RhoU, RhoB, and MRCKα (CDC42BPA)
361 expression. Closer examination of the data revealed that while the RhoB interaction was driven by
362 dependency under control conditions, PANC1 cells showed a shift in dependency towards RhoU and
363 MRCKα following RT, suggesting that they may play a role in driving RT-induced motility (Fig. 4A). We

364 used a second siRNA oligo sequence coupled with manually tracked subconfluent migration assays to
365 validate the dependency of irradiated PANC1 cells on MRCKα for motility (Fig. 4B(i), (ii)).
366
367 **The induction of spatially regulated MRCK signaling by RT is conserved *in vitro***
368 Metastasis is a leading cause of morbidity and mortality in pancreatic cancer and represents an urgent
369 and unmet clinical need. Given the availability of small-molecule inhibitors targeting MRCK, we
370 selected this kinase for further validation (35). Analysis of available patient datasets also indicated
371 that higher MRCKα mRNA expression showed a trend towards association with poorer overall survival
372 ($p = 0.059$; Fig. 5A(i)), unlike MRCKβ, which has no association with survival. MRCK and related kinases
373 are well described to be regulated by phosphorylation and intracellular location, which may explain
374 the weak interaction between outcome and RNA expression in patient datasets. In support of this,
375 preliminary single-cell RNA-seq data from KPC mice indicated a significant but minor increase in
376 MRCKα expression post RT (data not shown).
377 To explore this, we performed a western blot analysis to validate the biomarker of MRCK activity
378 (autophosphorylation of S1003; pMRCK; Fig. 5B). Using the PANC1 cell line, a highly motile cell line in
379 response to radiation (Fig 1C), we found no increase in pMRCK levels in response to 2 or 5 Gy RT (Fig
380 5C), suggesting that spatial regulation of RhoGTPase signaling may be a more useful determinant of
381 downstream signaling and the resultant phenotype. Therefore, we utilized high-throughput
382 immunofluorescence imaging with automated analysis to examine MRCK activity within different
383 cellular compartments. We demonstrated that MRCK activity significantly increased at the cell
384 membrane following irradiation across the two cell lines, indicating the induction of discrete cellular
385 responses to promote migration (Fig. 5C).
386
387 **Pharmacological targeting of MRCK with a small molecule inhibitor opposes radiation driven**
388 **migration**
389 We used a potent and specific small-molecule inhibitor of MRCK, BDP9066, to test the potential
390 therapeutic benefit of targeting MRCK in combination with RT in PDAC (35). The results in Fig. 6A (i) –
391 (iii) indicate that treatment of PANC1 cells with BDP9066 significantly reduced pMRCK at the cell
392 membrane only under irradiated conditions, demonstrating a shift towards MRCK dependency post
393 RT. ROCK inhibitor (Y27632) was used as a negative control. Furthermore, the data in Fig. 6A (iv)
394 revealed a dose-dependent reduction in pMRCK in response to BDP9066 with a EC50 10-fold lower in
395 irradiated cells. These data further indicated that the clinical use of MRCK inhibition may have the
396 greatest benefit when used in combination with RT. This radiation-specific reduction in pMRCK in
397 response to MRCK inhibition was confirmed in an additional cell line (Fig. 6B). Importantly,

398 subconfluent migration assays demonstrated that this reduction in MRCK activity translated into a
399 reduction in radiation-driven migration across a panel of cell lines. Of note, no effect on viability was
400 observed at the concentrations used in motility assays in two lines (1µM; Panc1, KPC). Interestingly,
401 the patient derived TKCC04 line was sensitive to BDP9066 under both control and irradiated conditions
402 indicating that in some conditions BDP9066 may have anti-tumorigenic properties in addition to
403 inhibiting local invasion (Fig. 6C).
404
405 **MRCK activity is upregulated at the invasive tumour margins and metastases post radiotherapy**
406 To determine whether MRCK activity was upregulated post RT *in vivo*, we stained the sections from
407 the KPC GEM model (Fig. 2) for pMRCK. While there was no increase in pMRCK across the tumor bulk
408 (Fig. 7A(i)), pMRCK was significantly upregulated at the tumor margins compared to that at the tumor
409 center (Fig. 7A (ii), (iii), (iv), (v)). Furthermore, this pattern of activation was concomitant with an
410 increase in Zeb1 expression (a marker of epithelial-to-mesenchymal transition; Fig. 7B). These data
411 indicate that RT may induce an MRCK-dependent, pro-invasive signature at the invasive borders of
412 PDAC tumors. Importantly, this increase in pMRCK was maintained in metastases from the
413 radiotherapy-treated cohort, indicating that MRCK signaling may be required to support progression
414 from local invasion to distant metastases (Fig 7C). Finally, using *ex vivo* cultured tumor tissue from KPC
415 GEM mice, we demonstrated that pMRCK levels, while not raised in response to RT across the tumour
416 section (mirroring the *in vivo* response described above), is significantly reduced by BDP9066 when
417 used in combination with RT, further highlighting the potential for therapeutic translation (Fig. 7D;
418 Supplemental M&M).
419 Together, our data indicate that RT drives increased metastasis in a clinically relevant model of PDAC,
420 with organotropism towards the lung. This is driven, at least in part, by upregulation of MRCK signaling.
421 Targeting MRCK with a small-molecule inhibitor may present a novel therapeutic avenue for
422 containing spread of disease during radiotherapy.

423

424 **Discussion**

425 Metastasis is a leading cause of morbidity and mortality in PDAC, with approximately 50% of patients
426 having metastasis at diagnosis, increasing to 90% upon autopsy (36). Identifying a therapeutic window
427 for the addition of anti-metastatic therapy has historically been a challenge for the cancer field. The
428 clear induction of metastasis by targeted radiotherapy in a clinically relevant model of PDAC provides
429 strong evidence for the first time that RT-driven metastasis may have an important clinical impact.
430 Importantly, we observed increased metastasis within a short timeframe post-RT (two weeks) in

431 animals that likely already had locally advanced disease at the time of treatment, mirroring the clinical
432 situation. These data indicate a clear window of opportunity for the addition of anti-metastatic
433 therapy concomitant with RT to control the dissemination rates and improve survival outcomes.
434 Indeed, constraining metastatic spread may be predicted to become increasingly urgent as better
435 methods for early, pre-metastatic detection of PDAC arise in the coming years. Although our data
436 provide an important advance in understanding the effect of RT on metastasis, to fully understand the
437 clinical relevance of our observations, the identification and analysis of outcome data from relevant
438 patient cohorts should be performed in the future.

439 Surprisingly, our data indicate that not only does RT drive metastasis, but also a switch in
440 organotropism towards the lungs. Although patients with isolated lung metastases have better
441 survival outcomes, our data clearly indicate a potential therapeutic window whereby the addition of
442 anti-metastatic therapy during RT may abrogate the metastatic spread of the disease and improve
443 survival (37). The observed lung organotropism also provides strong evidence for an RT-specific switch
444 in metastatic drivers. Indeed, our observation of increased pMRCK along with an increase in the
445 mesenchymal marker Zeb1 at the tumor borders indicates a cell signaling switch towards MRCK-driven
446 mesenchymal-like invasion during radiotherapy. Notably, single-cell RNA-seq data generated by our
447 team from irradiated KPC tumors did not identify a clear EMT signature, which may suggest that the
448 MRCK-driven response represents a partial EMT that is unique to the post RT scenario (data not
449 shown). Unpicking this signaling response in the future has the potential to not only further our
450 understanding of RT-driven metastasis but also of what drives lung-specific metastasis under
451 physiological conditions in solid cancers. In addition, the surprising conservation of this response
452 across cancers of starkly different origins (PDAC and glioblastoma) suggests that unpicking the
453 surrounding signaling cascades will further our understanding of radiobiological responses (23).

454 Previous studies have demonstrated that RT drives more fibrotic stroma in solid cancers, including
455 PDAC, which is largely driven by cancer-associated fibroblasts (CAFs) (9,38). This suggests that the
456 switch to mesenchymal-like migration may be a necessary adaptation that allows PDAC cells to locally
457 invade the post-RT landscape, resulting in increased metastatic spread. It is of interest that this switch
458 even occurs *in vitro* in the absence of a stromal compartment, perhaps suggesting that the PDAC cells
459 themselves have a key direct role in the deposition of fibrotic ECM post RT. Indeed, preliminary
460 secretomic and proteomic data from our group indicated that PDAC cells have an altered ECM
461 secretion profile post RT (data not shown).

462 Finally, we demonstrated the potential of utilizing this pro-metastatic switch in PDAC cells as a
463 therapeutic window through the addition of a small molecule inhibitor of MRCK. Although BDP9066

464 is well tolerated *in vivo*, its short plasma half-life limits its translational potential (35). The
465 development of a more stable iteration of the compound, or potentially the targeting of MRCK
466 through alternative approaches, such as PROTAC, is key to moving this approach towards the clinic.

467 In summary, our data highlight the impact of RT on the metastatic landscape of PDAC and identify a
468 novel, exploitable therapeutic approach to improve outcomes in patients with this cancer of current
469 unmet need in the future.

470

471 **Data Availability**

472 The authors confirm that the data supporting the findings of this study are available within the
473 manuscript and its supplementary materials or are available from the authors on request.

474 **Funding**

475 **JLB:** UK Research and Innovation Future Leaders Fellowship: MR/T04358X/1; Cancer Research UK
476 Radiation Research Centre of Excellence at the University of Glasgow: C16583/A28803. Beatson
477 Cancer Charity 24-25-091 **MT**: Pancreatic Cancer UK Career Foundation Fellowship
478 (CFF2022_08_Tesson). **JPM**: Cancer Research UK (A31287, A29996, CTRQQR-2021\100006, A25233),
479 and Pancreatic Cancer UK (2021RIF_28_Morton). **LMC**: CRUK (A17196, A31287, CTRQQR-
480 2021\100006, A23983, DRCRPG-Nov22/100007), UKRI MRC (MR/Y003365/1). **CM/RS**: Cancer
481 Research UK core funding to the CRUK Scotland Institute (A31287) and a core programme award to
482 CJM (A29801)

483

484

485 **Disclosure statement**

486 The Morton lab receives research funding from AstraZeneca, Avacta, Neobe, Redx Pharma, and UCB
487 Biopharma. The funding was not related to this study. LMC has consulted Ono Pharmaceuticals and is
488 an Academic Mentor to Team NST at the BioMed X Institute on work unrelated to this project.

489

490 **Author Contributions**

491 **Conception and design:** KMM, MT, JPM, JLB

492 **Development of methodology:** KMM, MT, MO, JPM, JLB, LMC, RC, JM, AJC and LMcG.

Acquisition of data (provided animals, acquired and managed patients, provided facilities, etc.): KM, MT, LD, RC, DG, SL, JM AJC, and YS

Analysis and interpretation of data (e.g., statistical analysis, biostatistics, computational analysis): KM, MT, LD, RC, DG, YS, SL, RS, CM, NM and JM

Writing, review, and/or revision of the manuscript: JLB, KM, JM, MO, and MT.

Acknowledgements

The histology was provided by the Histology facility of the CRUK-Scotland Institute. Imaging was provided by the Beatson Advanced Imaging Facility (RRID:SCR_023875) at the CRUK-Scotland Institute. *In vivo* support was provided by the Biological Service Unit of the CRUK Scotland Institute. Mass spectroscopy undertaken by the proteomics facility, CRUKSI and transcriptomics by the RNA sequencing facility, CRUKSI. Thank you to Prof. David Chang, Dr. Derek Grose and Dr. Aileen Dufton for lending their clinical insight into the review of this data.

References

1. Rawla P, Sunkara T, Gaduputi V. Epidemiology of Pancreatic Cancer: Global Trends, Etiology and Risk Factors. World J Oncol **2019**;10(1):10-27 doi 10.14740/wjon1166.
2. Rahib L, Wehner MR, Matrisian LM, Nead KT. Estimated Projection of US Cancer Incidence and Death to 2040. JAMA Netw Open **2021**;4(4):e214708 doi 10.1001/jamanetworkopen.2021.4708.
3. Kolbeinsson HM, Chandana S, Wright GP, Chung M. Pancreatic Cancer: A Review of Current Treatment and Novel Therapies. J Invest Surg **2023**;36(1):2129884 doi 10.1080/08941939.2022.2129884.
4. Versteijne E, Suker M, Groothuis K, Akkermans-Vogelaar JM, Besselink MG, Bonsing BA*, et al.* Preoperative chemoradiotherapy versus immediate surgery for resectable and borderline resectable pancreatic cancer: results of the Dutch randomized phase III PREOPANC trial. Journal of clinical oncology **2020**;38(16):1763-73.
5. Versteijne E, van Dam JL, Suker M, Janssen QP, Groothuis K, Akkermans-Vogelaar JM*, et al.* Neoadjuvant chemoradiotherapy versus upfront surgery for resectable and borderline resectable pancreatic cancer: long-term results of the Dutch randomized PREOPANC trial. Journal of Clinical Oncology **2022**;40(11):1220-30.
6. Hammel P, Huguet F, van Laethem J-L, Goldstein D, Glimelius B, Artru P*, et al.* Effect of chemoradiotherapy vs chemotherapy on survival in patients with locally advanced pancreatic cancer controlled after 4 months of gemcitabine with or without erlotinib: the LAP07 randomized clinical trial. Jama **2016**;315(17):1844-53.
7. Maxwell JE, Katz MHG. Radiotherapy for Resectable and Borderline Resectable Pancreas Cancer: When and Why? J Gastrointest Surg **2021**;25(3):843-8 doi 10.1007/s11605-020-04838-6.

533 8. Benkhaled S, Peters C, Jullian N, Arsenijevic T, Navez J, Van Gestel D*, et al.*
534 Combination, modulation and interplay of modern radiotherapy with the tumor
535 microenvironment and targeted therapies in pancreatic cancer: which candidates to
536 boost radiotherapy? Cancers **2023**;15(3):768.
537 9. Tesson M, Morton JP. The preclinical gap in pancreatic cancer and radiotherapy. Dis
538 Model Mech **2024**;17(7) doi 10.1242/dmm.050703.
539 10. Lee SY, Jeong EK, Ju MK, Jeon HM, Kim MY, Kim CH*, et al.* Induction of metastasis,
540 cancer stem cell phenotype, and oncogenic metabolism in cancer cells by ionizing
541 radiation. Molecular cancer **2017**;16:1-25.
542 11. Blyth BJ, Cole AJ, MacManus MP, Martin OA. Radiation therapy-induced metastasis:
543 radiobiology and clinical implications. Clinical & experimental metastasis
544 **2018**;35:223-36.
545 12. Vilalta M, Rafat M, Graves EE. Effects of radiation on metastasis and tumor cell
546 migration. Cellular and Molecular Life Sciences **2016**;73:2999-3007.
547 13. Li D, Qu C, Ning Z, Wang H, Zang K, Zhuang L*, et al.* Radiation promotes epithelial-to-
548 mesenchymal transition and invasion of pancreatic cancer cell by activating
549 carcinoma-associated fibroblasts. Am J Cancer Res **2016**;6(10):2192-206.
550 14. Fujita M, Imadome K, Endo S, Shoji Y, Yamada S, Imai T. Nitric oxide increases the
551 invasion of pancreatic cancer cells via activation of the PI3K-AKT and RhoA pathways
552 after carbon ion irradiation. FEBS Lett **2014**;588(17):3240-50 doi
553 10.1016/j.febslet.2014.07.006.
554 15. Zeng RJ, Zheng CW, Chen WX, Xu LY, Li EM. Rho GTPases in cancer radiotherapy and
555 metastasis. Cancer Metastasis Rev **2020**;39(4):1245-62 doi 10.1007/s10555-020-
556 09923-5.
557 16. Hall A, Nobes CD. Rho GTPases: molecular switches that control the organization and
558 dynamics of the actin cytoskeleton. Philos Trans R Soc Lond B Biol Sci
559 **2000**;355(1399):965-70 doi 10.1098/rstb.2000.0632.
560 17. Hodge RG, Ridley AJ. Regulating Rho GTPases and their regulators. Nature reviews
561 Molecular cell biology **2016**;17(8):496-510.
562 18. Unbekandt M, Olson MF. The actin-myosin regulatory MRCK kinases: regulation,
563 biological functions and associations with human cancer. J Mol Med (Berl)
564 **2014**;92(3):217-25 doi 10.1007/s00109-014-1133-6.
565 19. Rath N, Olson MF. Rho-associated kinases in tumorigenesis: re-considering ROCK
566 inhibition for cancer therapy. EMBO Rep **2012**;13(10):900-8 doi
567 10.1038/embor.2012.127.
568 20. Pankova K, Rosel D, Novotny M, Brabek J. The molecular mechanisms of transition
569 between mesenchymal and amoeboid invasiveness in tumor cells. Cell Mol Life Sci
570 **2010**;67(1):63-71 doi 10.1007/s00018-009-0132-1.
571 21. Talkenberger K, Cavalcanti-Adam EA, Voss-Bohme A, Deutsch A. Amoeboid-
572 mesenchymal migration plasticity promotes invasion only in complex heterogeneous
573 microenvironments. Sci Rep **2017**;7(1):9237 doi 10.1038/s41598-017-09300-3.
574 22. Gadea G, de Toledo M, Anguille C, Roux P. Loss of p53 promotes RhoA-ROCK-
575 dependent cell migration and invasion in 3D matrices. J Cell Biol **2007**;178(1):23-30
576 doi 10.1083/jcb.200701120.
577 23. Birch JL, Strathdee K, Gilmour L, Vallatos A, McDonald L, Kouzeli A*, et al.* A Novel
578 Small-Molecule Inhibitor of MRCK Prevents Radiation-Driven Invasion in
579 Glioblastoma. Cancer Res **2018**;78(22):6509-22 doi 10.1158/0008-5472.can-18-1697.

24. Dreyer SB, Upstill-Goddard R, Paulus-Hock V, Paris C, Lampraki EM, Dray E*, et al.* Targeting DNA Damage Response and Replication Stress in Pancreatic Cancer. Gastroenterology **2021**;160(1):362-77.e13 doi 10.1053/j.gastro.2020.09.043.
25. Pachitariu M, Stringer C. Cellpose 2.0: how to train your own model. Nat Methods **2022**;19(12):1634-41 doi 10.1038/s41592-022-01663-4.
26. Stringer C, Wang T, Michaelos M, Pachitariu M. Cellpose: a generalist algorithm for cellular segmentation. Nat Methods **2021**;18(1):100-6 doi 10.1038/s41592-020-01018-x.
27. Ulicna K, Vallardi G, Charras G, Lowe AR. Automated Deep Lineage Tree Analysis Using a Bayesian Single Cell Tracking Approach. Frontiers in Computer Science **2021**;3 doi 10.3389/fcomp.2021.734559.
28. Hingorani SR, Wang L, Multani AS, Combs C, Deramaudt TB, Hruban RH*, et al.* Trp53R172H and KrasG12D cooperate to promote chromosomal instability and widely metastatic pancreatic ductal adenocarcinoma in mice. Cancer Cell **2005**;7(5):469-83 doi 10.1016/j.ccr.2005.04.023.
29. Tesson M, Stevenson K, Karim SA, Nixon C, Chalmers AJ, Sansom OJ*, et al.* Targeted irradiation in an autochthonous mouse model of pancreatic cancer. Dis Model Mech **2024**;17(3) doi 10.1242/dmm.050463.
30. Bankhead P, Loughrey MB, Fernandez JA, Dombrowski Y, McArt DG, Dunne PD*, et al.* QuPath: Open source software for digital pathology image analysis. Sci Rep **2017**;7(1):16878 doi 10.1038/s41598-017-17204-5.
31. Chastney MR, Kaivola J, Leppanen VM, Ivaska J. The role and regulation of integrins in cell migration and invasion. Nat Rev Mol Cell Biol **2025**;26(2):147-67 doi 10.1038/s41580-024-00777-1.
32. Fujita M, Otsuka Y, Imadome K, Endo S, Yamada S, Imai T. Carbon-ion radiation enhances migration ability and invasiveness of the pancreatic cancer cell, PANC-1, in vitro. Cancer Sci **2012**;103(4):677-83 doi 10.1111/j.1349-7006.2011.02190.x.
33. Ohuchida K, Mizumoto K, Murakami M, Qian L-W, Sato N, Nagai E*, et al.* Radiation to stromal fibroblasts increases invasiveness of pancreatic cancer cells through tumor-stromal interactions. Cancer research **2004**;64(9):3215-22.
34. Qian LW, Mizumoto K, Urashima T, Nagai E, Maehara N, Sato N*, et al.* Radiation-induced increase in invasive potential of human pancreatic cancer cells and its blockade by a matrix metalloproteinase inhibitor, CGS27023. Clin Cancer Res **2002**;8(4):1223-7.
35. Unbekandt M, Belshaw S, Bower J, Clarke M, Cordes J, Crighton D*, et al.* Discovery of Potent and Selective MRCK Inhibitors with Therapeutic Effect on Skin Cancer. Cancer Res **2018**;78(8):2096-114 doi 10.1158/0008-5472.can-17-2870.
36. Zhang L, Jin R, Yang X, Ying D. A population-based study of synchronous distant metastases and prognosis in patients with PDAC at initial diagnosis. Front Oncol **2023**;13:1087700 doi 10.3389/fonc.2023.1087700.
37. Levine JM, Rompen IF, Franco JC, Swett B, Kryschi MC, Habib JR*, et al.* The impact of metastatic sites on survival Rates and predictors of extended survival in patients with metastatic pancreatic cancer. Pancreatology **2024**;24(6):887-93 doi 10.1016/j.pan.2024.06.004.
38. Blyth BJ, Cole AJ, MacManus MP, Martin OA. Radiation therapy-induced metastasis: radiobiology and clinical implications. Clin Exp Metastasis **2018**;35(4):223-36 doi 10.1007/s10585-017-9867-5.

627

628

Figure. 1 McLay *et al*

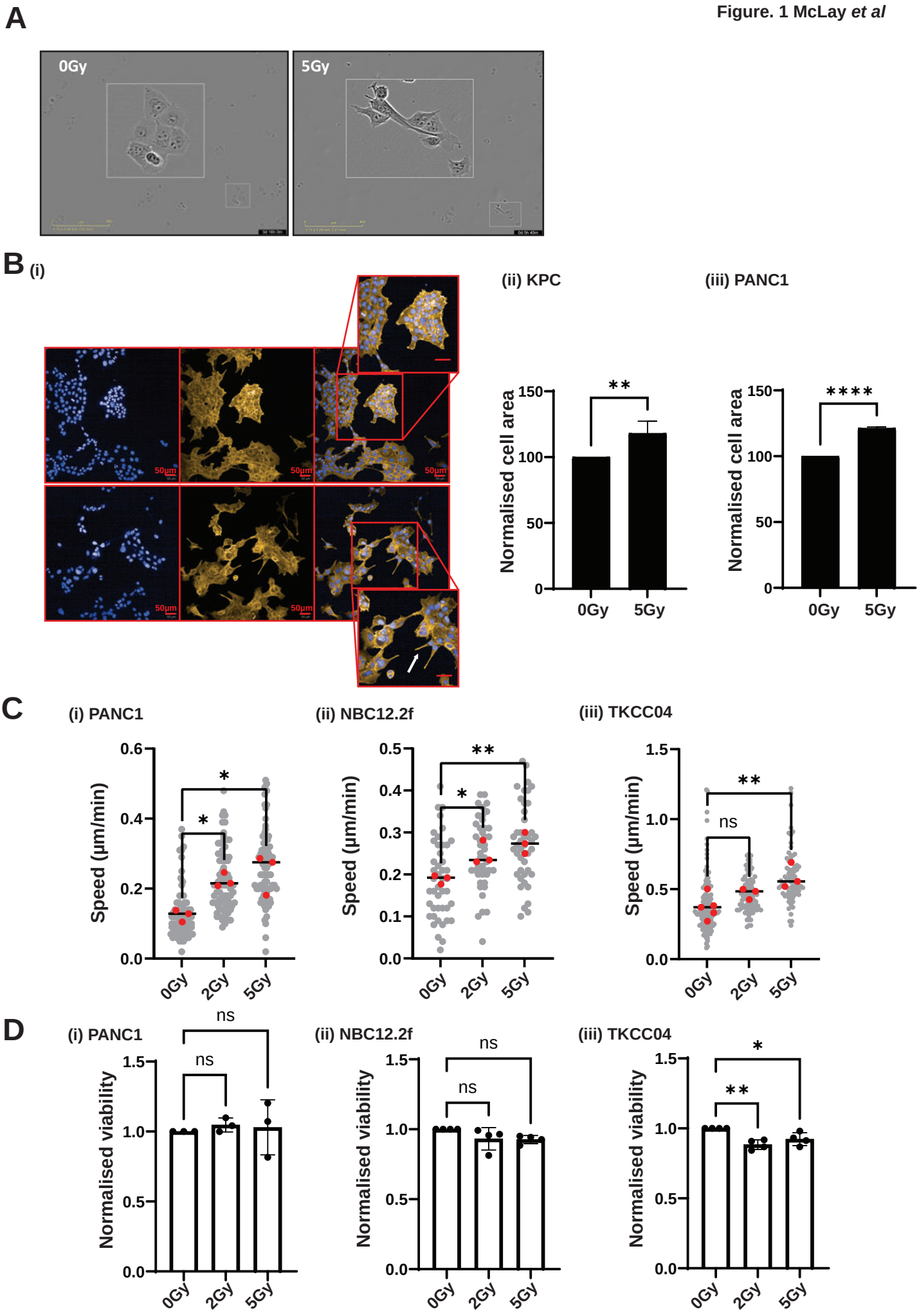

Fig 1.

Radiotherapy induces cell motility across a panel of PDAC cell lines. A) PANC1 cells imaged under phase contrast indicating morphology shift following exposure to 5 Gy RT. **B) (i)** PDAC cells treated with either 0 Gy or 5 Gy RT and imaged via high-throughput imaging. (Blue, DAPI; yellow, actin; last panel, merge) followed by automated analysis of cell area **(ii)** KPC (NBC12.2f) **(iii)** PANC1. Scale bar, 50 µm. Data derived from three independent experiments each containing 4 internal replicates, >1000 cells measured per condition per independent experiment. Error bars = Standard Deviation. Statistical analysis: two-tailed, unpaired *t* test. **, $P < 0.01$; ****, $P < 0.0001$. **C) (i)** PANC1 **(ii)** NBC12.2f (KPC) and **(iii)** TKCC04 cells treated with 0, 2 or 5 Gy RT followed by subconfluent migration assay 24 hrs post RT using time-lapse microscopy and single cell tracking to quantify migration speed. Individual cell speeds plotted in grey, means from independent experiments plotted in red, mean from independent repeats = horizontal bar. Statistical analysis: One-way ANOVA; ns, not significant, *, $P < 0.05$, ** $P < 0.01$. **D)** Viability assays conducted 24hrs post RT on **(i)** PANC1 **(ii)** NBC12.2f and **(iii)** TKCC04. Data from three independent experiments for each cell line. Statistical analysis: One-way ANOVA; ns, not significant, *, $P < 0.05$, ** $P < 0.01$.

Table 1: Migration speed responses to 2 or 5 Gy in a panel of PDAC cell lines.

		2Gy		5Gy	
Cell line	**Origin**	**Δ speed**	**P value**	**Δ speed**	**P value**
PANC1	Commercial	1.822849	0.0027	1.98868	0.0024
Miapaca2	Commercial	1.07396	0.6494	1.019541	0.8727
ASPC1	Commercial	0.879926	0.3841	1.267169	0.0658
NBC12.2f	Murine (KPC)	1.317871	0.0163	1.451858	0.0002
NBC12.2g	Murine (KPC)	1.327689	0.0618	1.044459	0.7157
NBC13.3a	Murine (KPC)	1.692982	<0.0001	2.056329	0.0049
TKC004	Primary patient derived	1.455445	0.0085	1.413566	<0.0001
TKC005	Primary patient derived	1.58574	0.0137	1.558938	0.0099

Table 1.

Migration speed responses to 2 or 5 Gy in a panel of PDAC cell lines.

The migration speed was normalized to 0 Gy to determine the fractional change. Statistical analysis: Student's t-test. Green cells: significant increase in speed post RT, blue cells: trend towards increase, white cells: no increase. Data were obtained from three biological replicates for each cell line.

Figure. 2 McLay *et al*

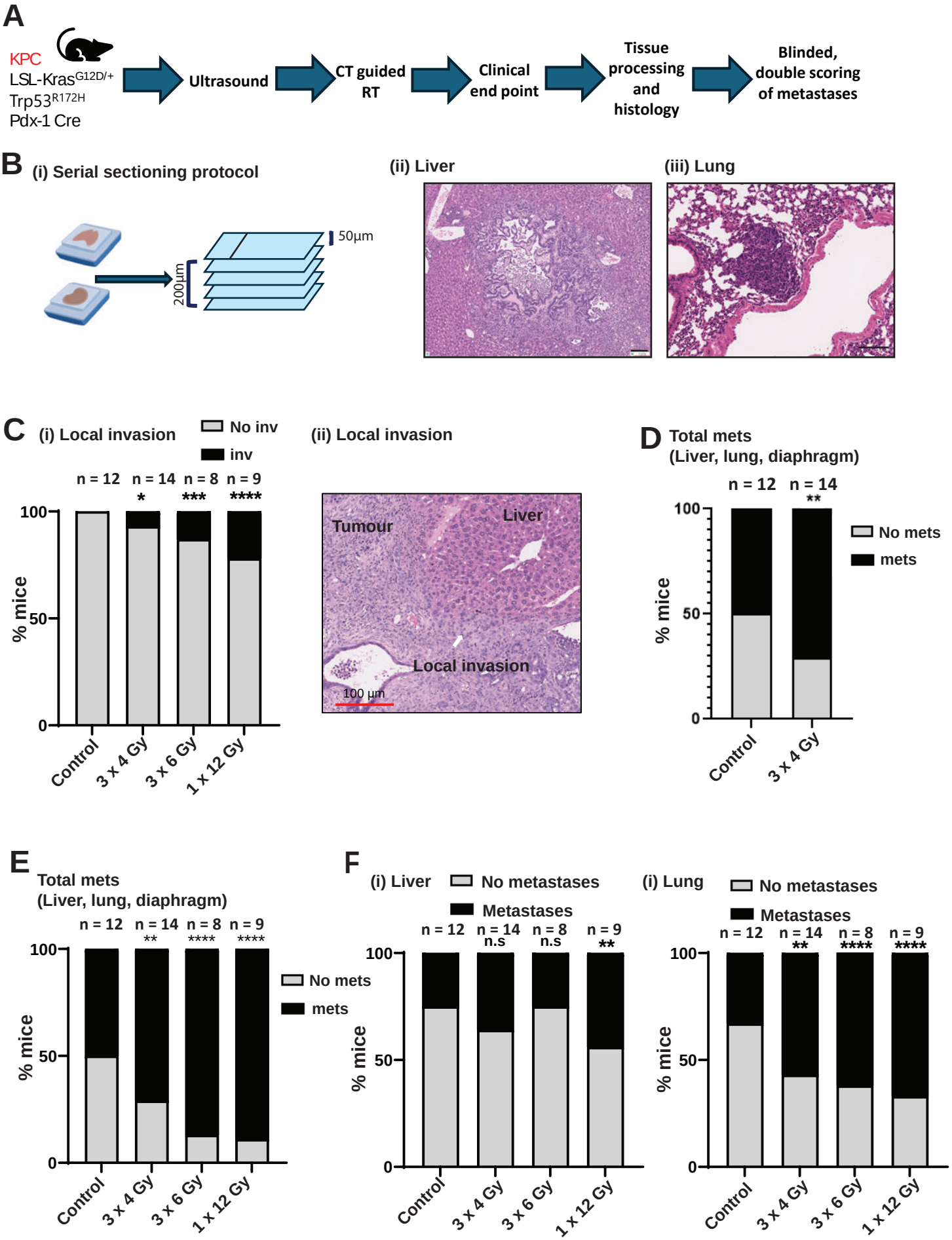

Fig 2.

Radiotherapy increases the metastatic burden of pancreatic cancer in a clinically relevant genetic mouse model. A) Tumour bearing KPC mice were subjected to CT-guided targeted RT and sampled at clinical endpoint. Liver and lung sections were blinded and double scored for presence of metastases. **B) (i)** Serial sectioning protocol **(ii)**, **(iii)** example images of liver and lung metastases. **C)** i) H&E sections from KPC mice treated with 0Gy, 3x4Gy, 3x6Gy or 1x12Gy were scored for the presence of local invasion (example in (ii)). **D)** H&E liver, lung, and diaphragm sections from KPC mice treated with 0 or 3x4Gy RT were assessed for presence of metastases. **E)** Metastasis scoring across multiple RT protocols, as indicated. **F)** Breakdown of metastases present in liver **(i)** or lung **(ii)**. Number per cohort indicated on graphs. Statistical analysis: Chi-square test. ns, non-significant, *, $P < 0.05$, **, $P < 0.01$, ***, $P < 0.001$ ****, $P < 0.0001$.

Figure 3. McLay *et al*

A

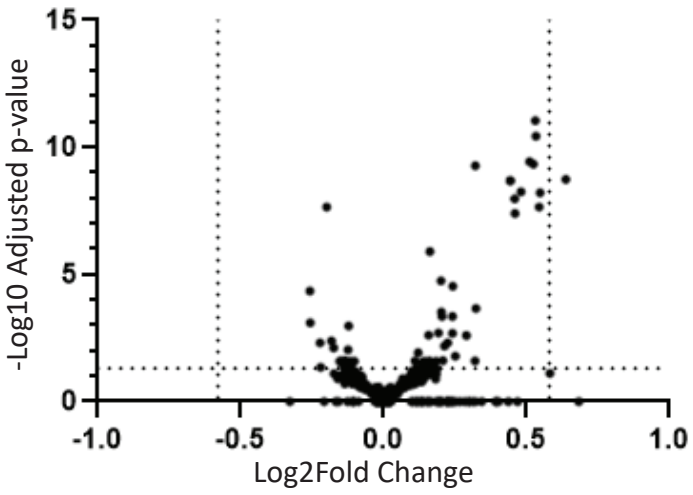

B

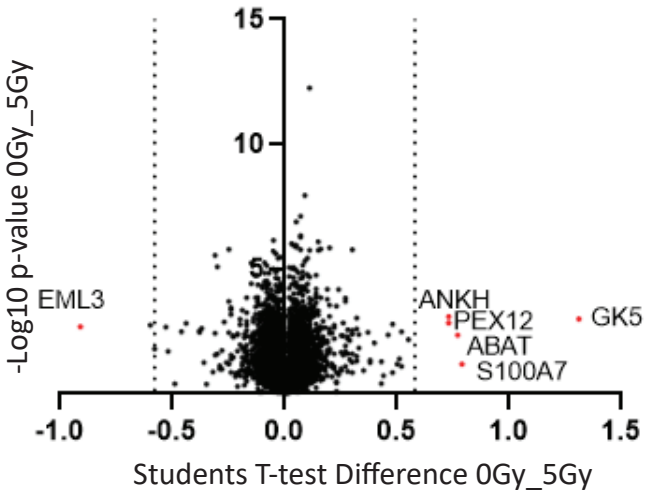

C (i)

	MRCKb	RhoA	ROCK1	GAPDH
NT	1.00	1.00	1.00	1.00
MRCK KD	0.43	0.89	0.76	1.02
RhoA KD	1.17	0.54	0.58	1.01
ROCK1 KD	1.09	0.67	0.56	0.96
GAPDH KD	2.64	1.10	1.73	0.51

(ii)

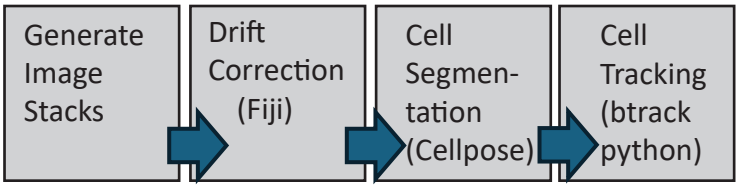

(iii)

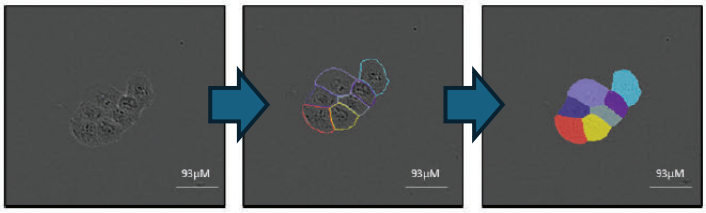

D

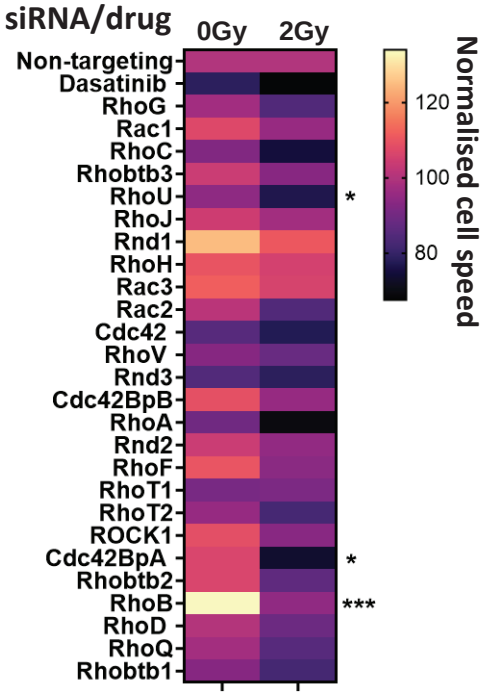

Fig 3.

Dependence of RT induced motility on members of the RhoGTPase signaling family.

A-B) Differential gene expression (DGE) was analysed 24 hrs post treatment with 0 or 5Gy RT in three biological replicates (independently derived KPC lines, NBC12.2f, NBC12.2g and NBC13.3a). The proteome of PANC1 cells was analysed using a tandem mass tag approach 6 hrs post treatment with 0 or 5Gy RT**. C (i)** Efficacy of knockdown was confirmed by western blotting for several targets. Expression normalized to actin loading control and shown as ratio of non-targeted control treated cells (NT). Example blot in Fig. S3. **(ii)** Automated cell tracker workflow. Generation of image stacks and application of drift correction via plugin in Fiji followed by cell segmentation using cellpose 2.0 and tracks cells using btrack python package. **(iii)** representative image of cell segmentation from cellpose 2.0. **D)** RhoGTPase siRNA motility screen targeting all members of the RhoGTPase signaling family and select effector kinases in PANC1 cells exposed to either 0 or 5 Gy RT. Presented as a heatmap where each cell speed is normalised to non-targeting control siRNA from the match condition (0 or 5Gy). Statistical analysis: Two-way ANOVA. *, $P < 0.05$, ***, $P < 0.001$. Statistical analysis: two-tailed, unpaired *t* test. ns, non-significant, *, $P < 0.05$, **, $P < 0.01$; ****, $P < 0.0001$.

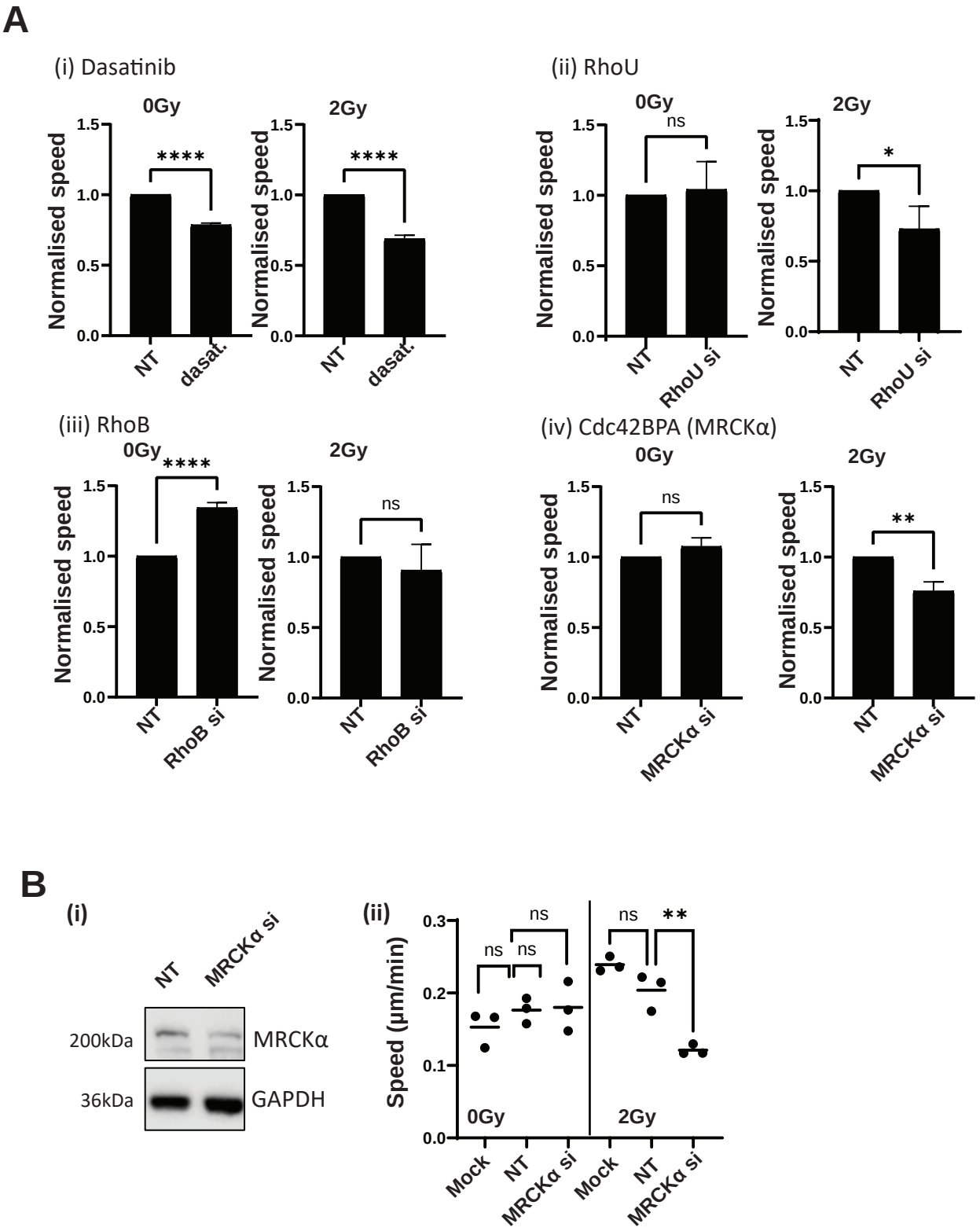
A
(i) Dasatinib
0Gy
2Gy
Normalised speed
1.5
1.0
0.5
0.0
****
NT
dasat.
(ii) RhoU
ns
*
RhoU si
(iii) RhoB
RhoB si
(iv) Cdc42BPA (MRCKα)
**
MRCKα si
B
(i)
NT
MRCKα si
200kDa
MRCKα
36kDa
GAPDH
(ii)
Speed (µm/min)
0.3
0.2
0.1
0.0
ns
**
0Gy
2Gy
Mock
NT
MRCKα si

Fig 4.

RT-induced motility is dependent on MRCK and RhoU

A) Normalised cell speeds of identified hits from the RhoGTPase siRNA screen. **(i)** Dasatinib (positive control) **(ii)** RhoU **(iii)** RhoB and **(iv)** Cdc42BPA (MRCKα). All data from 3 independent experiments with >50 cells tracked per condition per experiment. **B)** PANC1 cells transfected with an alternate siRNA targeting MRCKα followed by **(i)** Confirmation of MRCKα knockdown via western blotting and **(ii)** subconfluent migration assay. N=3 independent repeats, horizontal bar = mean. Statistical analysis: one-way ANOVA. ns, non-significant, **, $P < 0.01$.

Figure. 5 McLay *et al*

A

(i) Cdc42BPA (MRCKα) (ii) Cdc42BPB (MRCKβ)

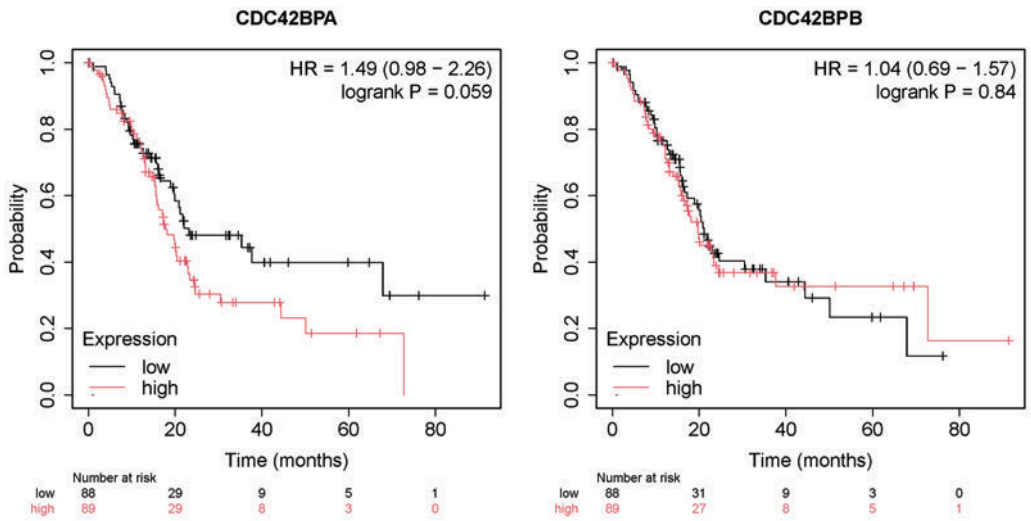

B (i)

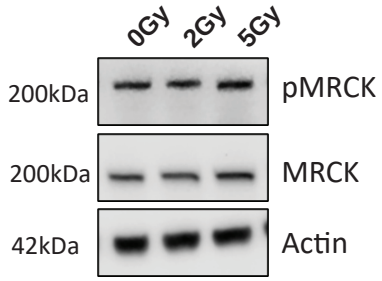

C (i)

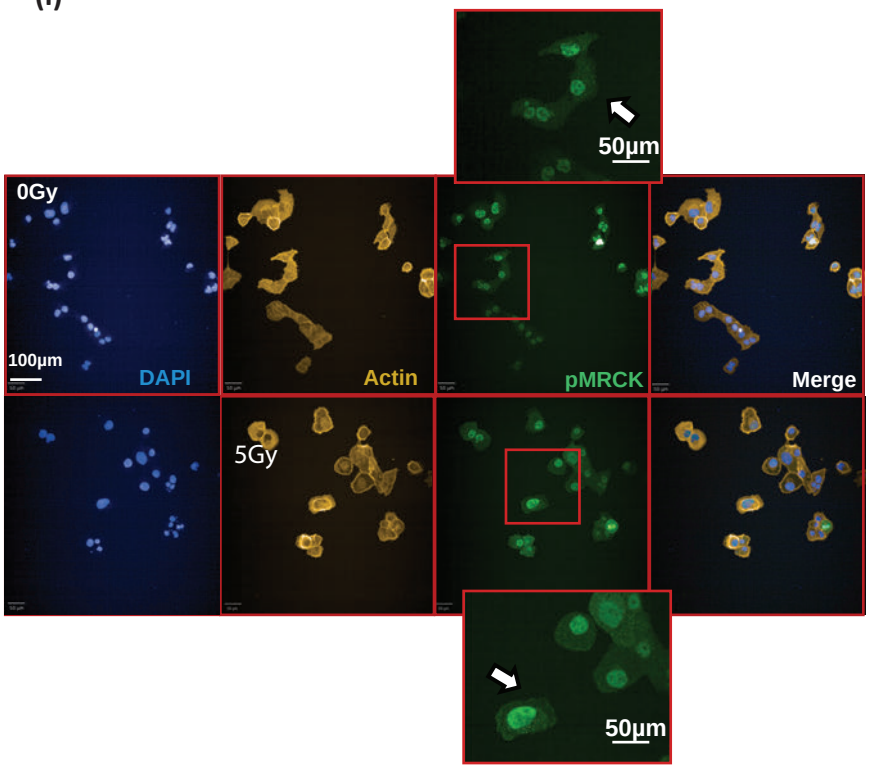

(ii) PANC1

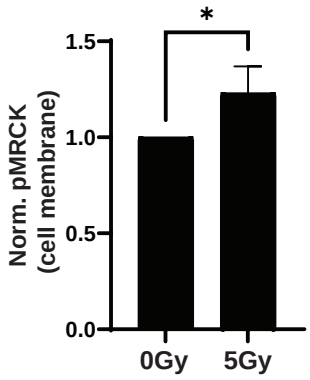

(iii) KPC

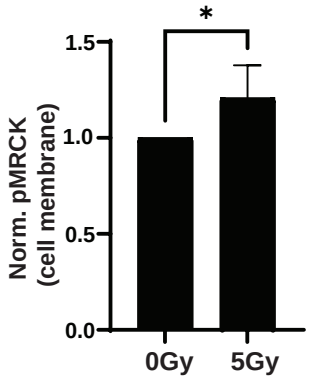

Fig. 5.
MRCK signaling is spatially regulated by RT *in vitro*

A) CDC42BPA (i) and CDC42BPB (ii) mRNA expression and overall survival from available patient datasets plotted using kmplot.com. 177 samples with a median expression cut off. **B)** PANC1 cells treated with 0, 2Gy or 5Gy followed by western blotting of pMRCK total MRCK and actin (loading control). **C) (i)** PANC1 cells treated with either 0 Gy or 5 Gy RT followed by IF for pMRCK and high throughput confocal imaging. Blue, DAPI; yellow, actin; green, pMRCK; last panel, merge. Scale bar, 100 µm. (ii) automated image analysis of membrane associated pMRCK in **(ii)** PANC1 **(iii)** KPC (NBC12.2f) cells exposed to 0 or 2 Gy. All data from 3 independent repeats. Statistical analysis, Students T Test. * $P < 0.05$.

Figure. 6 McLay *et al*

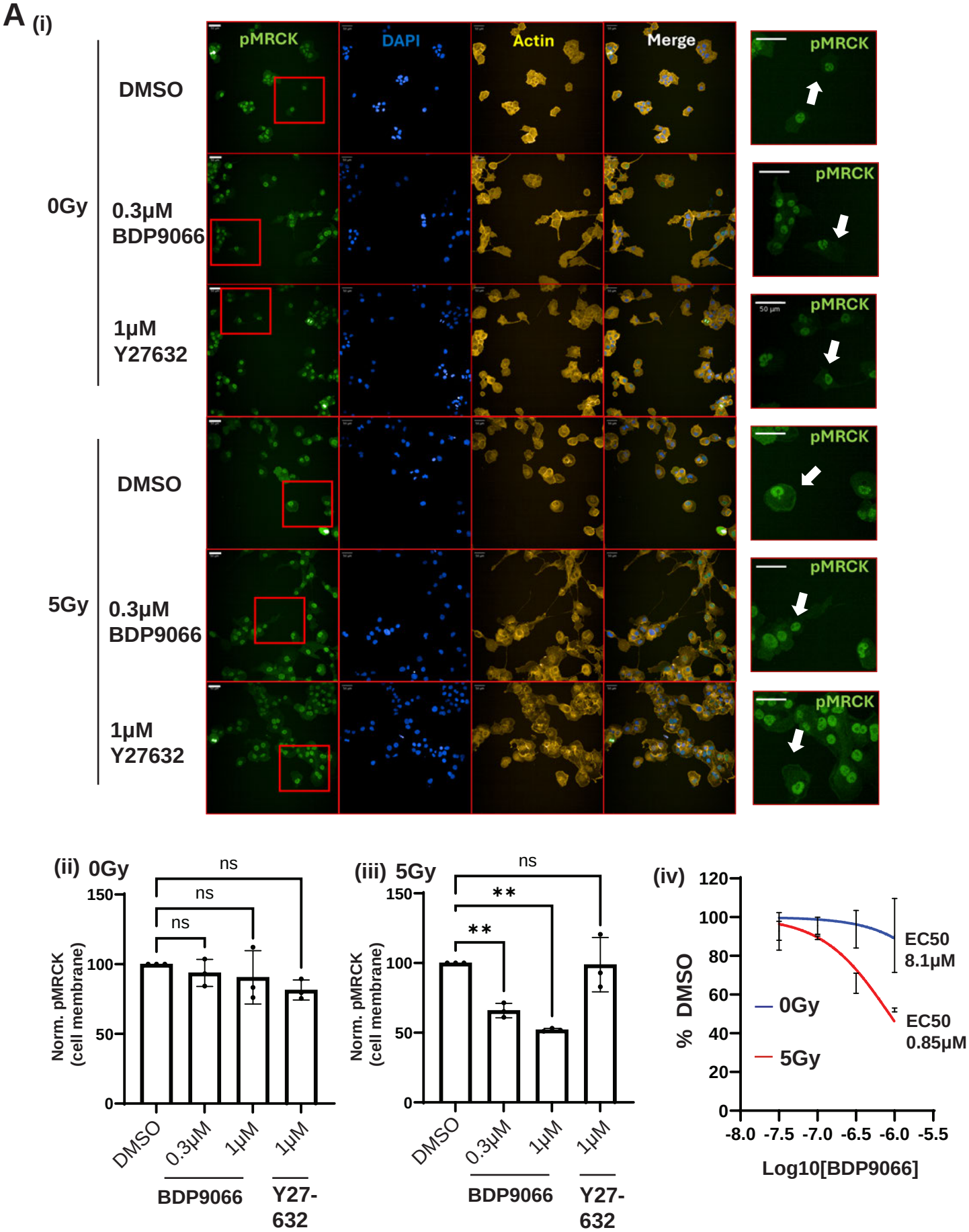

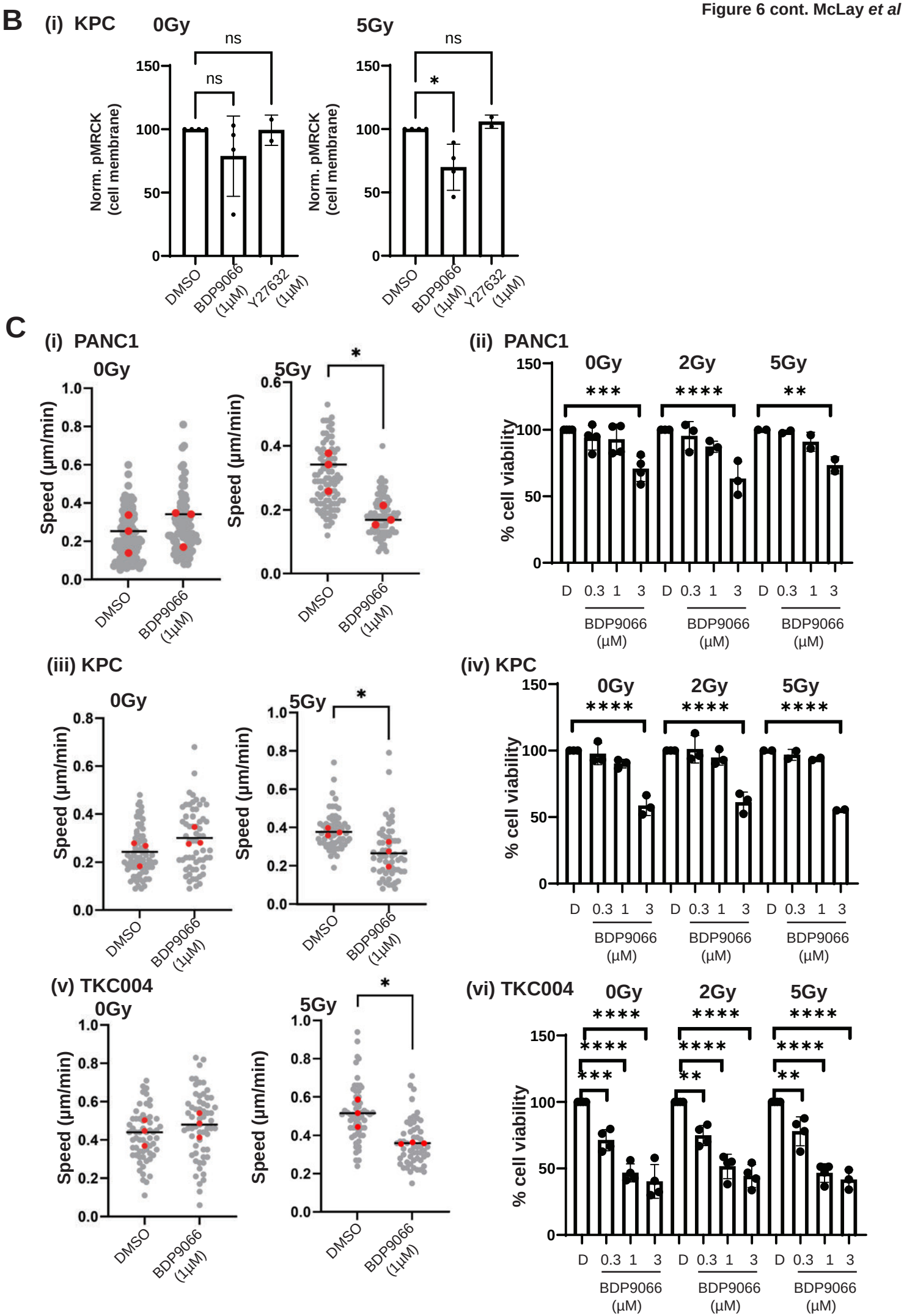
B
(i) KPC
0Gy
5Gy
ns
ns
*
Norm. pMRCK (cell membrane)
150
100
50
0
DMSO
BDP9066 (1μM)
Y27632 (1μM)
C
(i) PANC1
0Gy
5Gy
Speed (μm/min)
DMSO
BDP9066 (1μM)
(ii) PANC1
0Gy
2Gy
5Gy
***
****
**
% cell viability
D 0.3 1 3 D 0.3 1 3 D 0.3 1 3
BDP9066 (μM)
(iii) KPC
(iv) KPC
(v) TKC004
(vi) TKC004

Fig 6.

Pharmacological targeting of MRCK opposes radiation driven migration

A) (i) PANC1 cells treated with either 0 Gy or 5 Gy +/- DMSO, BDP9066 or Y27632 followed by high-throughput imaging. Blue, DAPI; yellow, actin; green, pMRCK; last panel, merge. Scale bar, 100 µm. White arrows indicate cell membrane. (ii)-(iii) Automated analysis of membrane associated pMRCK from (i). (iv) Dose response curve in the presence/absence of RT (5Gy). All data from 3 independent repeats. Statistical analysis: one-way ANOVA. ns, non-significant, **, $P < 0.01$. **B)** Automated analysis of membrane associated pMRCK in KPC (NBC12.2f) cells. Statistical analysis: one-way ANOVA. ns, non-significant, *, $P < 0.05$. Data from 3 independent experiments, error bars = standard deviation. **C)** Subconfluent migration and cell viability assays using (i)-(ii) PANC1, (iii)-(iv) KPC and (v)-(vi) TKC004 cells to measure the response to BDP9066 in the presence/absence of RT (5Gy). 0Gy and 5 Gy plotted separately due to experiment design. All data from 3 independent repeats. Statistical analysis: two-tailed, unpaired *t* test (motility) or one way anova (viability). *, $P < 0.05$ **, $P < 0.01$ ***, $P < 0.005$, ****, $P < 0.001$

Figure. 7 McLay *et al*

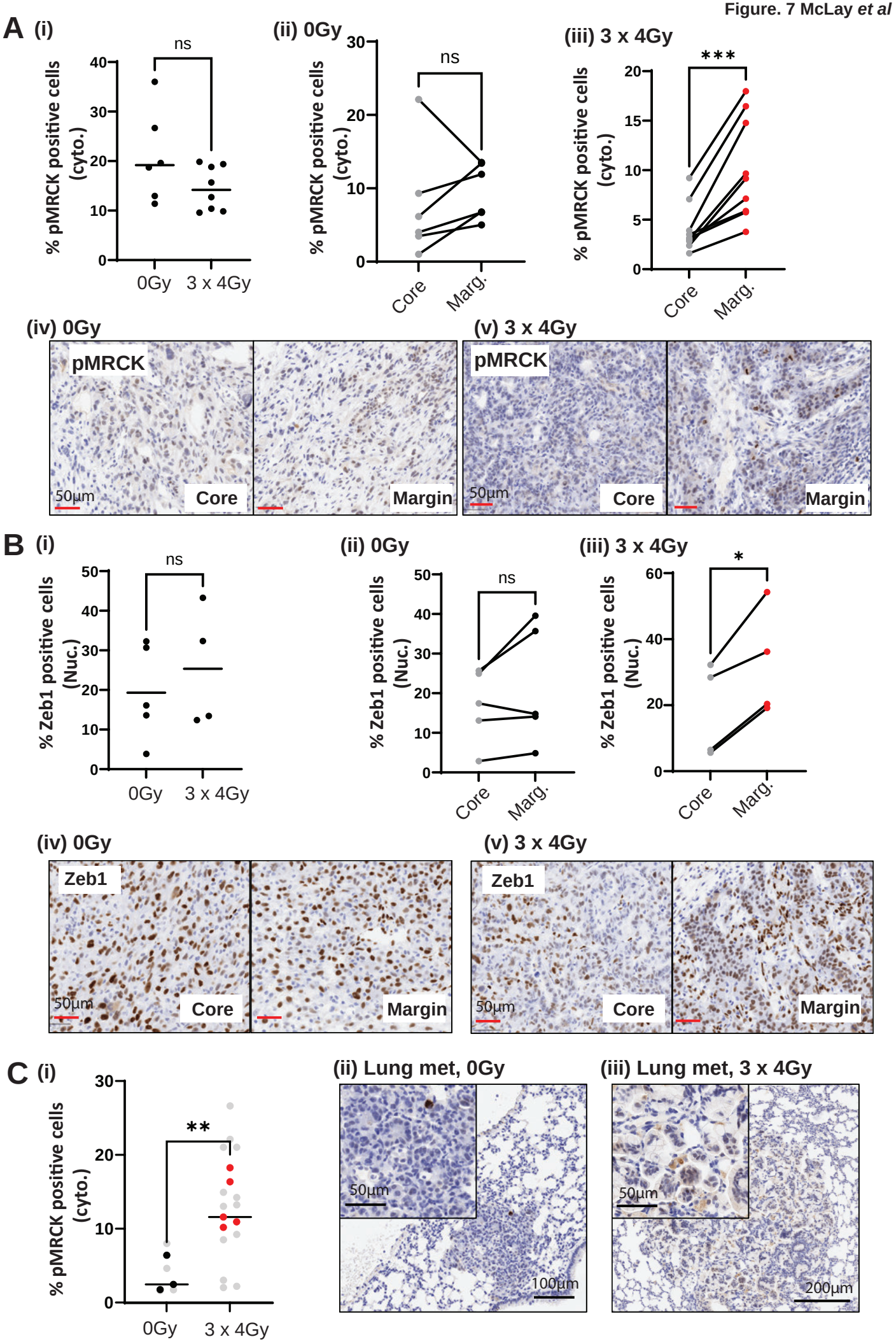

D

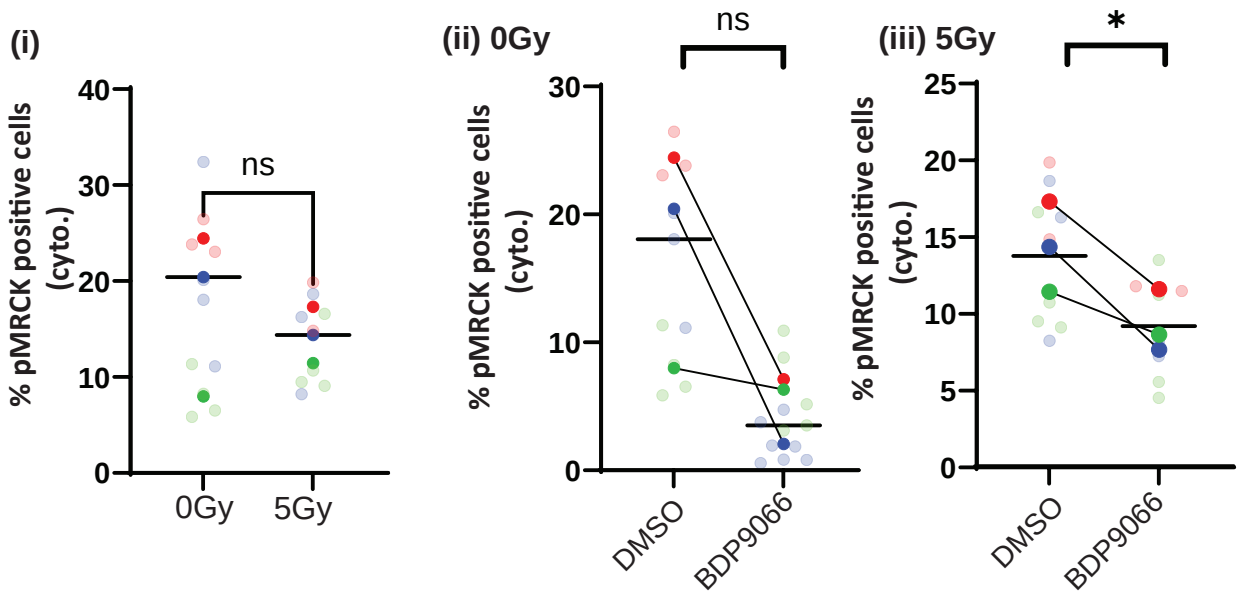

(iv) 5Gy DMSO

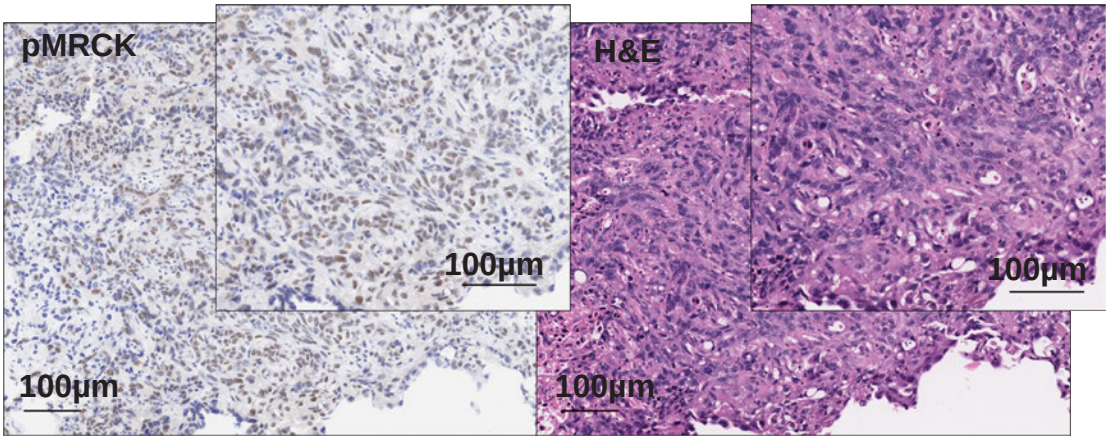

(v) 5Gy 3µM BDP9066

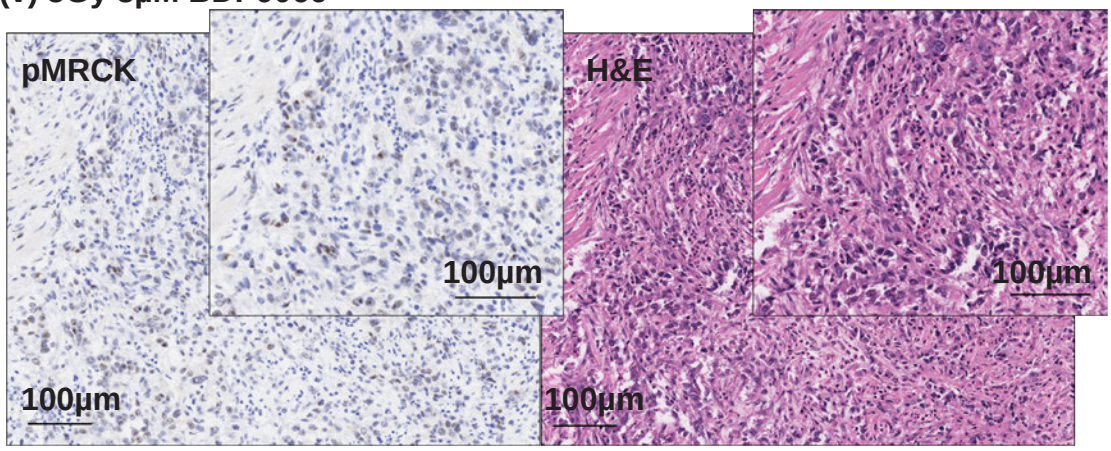

Fig 7.

MRCK activity is upregulated at invasive tumour margins post radiotherapy *in vivo*

A) (i) Percentage of cytoplasmic pMRCK positive cells in KPC tumours treated with either 0 Gy or 3 x 4 Gy, n=6 and 8 mice, respectively. (ii, iii) Percentage of cytoplasmic pMRCK positive cells in the core v margin of KPC tumours treated with 0 Gy (ii) or 3 x 4Gy (iii). Means from individual tumours plotted. (iv, v) Example images from (ii)-(iii). Statistical analysis: two-tailed, unpaired *t* test. ns, non-significant, ***, $P < 0.001$. **B)** (i) Percentage of nuclear ZEB1 positive cells in KPC tumours treated with either 0 Gy or 3 x 4 Gy. (ii, iii) Percentage of nuclear Zeb1 positive cells in the core v margin of KPC tumours treated with 0 Gy (ii) or 3 x 4Gy (iii). (iv, v) Example images from (ii)-(iii). Means from individual mice plotted, n=5 0Gy, n=4 3x4Gy. Statistical analysis: two-tailed, unpaired *t* test. ns, non-significant, *, $P < 0.05$. **C)** (i) Percentage of cytoplasmic pMRCK positive cells in liver and lung metastases from KPC mice treated with 0 Gy or 3 x 4 Gy. Individual metastases from mice plotted in grey. Average per mouse in black/red. Statistical analysis: two-tailed, unpaired *t* test. *, $P < 0.05$. (ii, iii) Example images from (i). **D)** Percentage of pMRCK positive cells (cytoplasmic) in sections of 300µm slices from KPC tumours cultured *ex vivo* treated with 0 or 5Gy alone (i) or in combination with DMSO or BDP9066 (ii)-(ii), n=3 mice per group. (iv), (v) exemplar images. Statistical analysis: paired t test, ns, non-significant, *, $P < 0.05$. Means from individual experiments plotted as bold data points. Internal replicate data points plotted in corresponding transparent data points.